

Spectroscopy of hot γ Doradus and A–F hybrid *Kepler* candidates close to the hot border of the δ Scuti instability strip

F. Kahraman Aliçavuş^{1,2★}, E. Poretti^{3,4★}, G. Catanzaro⁵, B. Smalley⁶,
E. Niemczura⁷, M. Rainer^{3,8} and G. Handler¹

¹*Nicolaus Copernicus Astronomical Center, Bartycka 18, PL-00-716 Warsaw, Poland*

²*Çanakkale Onsekiz Mart University, Faculty of Sciences and Arts, Physics Department, 17100, Çanakkale, Turkey*

³*INAF – Osservatorio Astronomico di Brera, via E. Bianchi 46, I-23807 Merate (LC), Italy*

⁴*INAF – Fundación Galileo Galilei, Rambla José Ana Fernández Pérez 7, E-38712 Breña Baja, TF, Spain*

⁵*INAF – Osservatorio Astrofisico di Catania, Via S. Sofia 78, I-95123 Catania, Italy*

⁶*Astrophysics Group, Keele University, Staffordshire, ST5 5BG, UK*

⁷*Instytut Astronomiczny, Uniwersytet Wrocławski, ul. Kopernika 11, PL-51-622 Wrocław, Poland*

⁸*INAF – Osservatorio Astrofisico di Arcetri Largo E. Fermi 5, I-50125 Firenze, Italy*

Accepted 2020 February 4. Received 2020 January 16; in original form 2019 September 7

ABSTRACT

If γ Dor-type pulsations are driven by the convective blocking mechanism, a convective envelope at a sufficient depth is essential. There are several hot γ Dor and hybrid star candidates in which there should not be an adequate convective envelope to excite the γ Dor-type oscillations. The existence of these hot objects needs an explanation. Therefore, we selected, observed, and studied 24 hot γ Dor and hybrid candidates to investigate their properties. The atmospheric parameters, chemical abundances, and $v \sin i$ values of the candidates were obtained using medium-resolution ($R = 46\,000$) spectra taken with the Fibre-fed Échelle Spectrograph instrument mounted at the *Nordic Optical Telescope*. We also carried out frequency analyses of the *Kepler* long- and short-cadence data to determine the exact pulsation contents. We found only five bona fide hot γ Dor and three bona fide hot hybrid stars in our sample. The other 16 stars were found to be normal γ Dor, δ Sct, or hybrid variables. No chemical peculiarity was detected in the spectra of the bona fide hot γ Dor and hybrid stars. We investigated the interplay between rotation and pulsational modes. We also found that the hot γ Dor stars have higher *Gaia* luminosities and larger radii compared to main-sequence A–F stars.

Key words: stars: abundances – stars: atmospheres – stars: general – stars: oscillations – stars: rotation.

1 INTRODUCTION

The *Kepler* spacecraft (Borucki et al. 2010; Koch et al. 2010) was originally launched to detect Earth-like transiting planets, but it also shed new light on many other aspects of stellar astrophysics (e.g. Compton, Bedding & Stello 2019; Helminiak et al. 2019; Pizzocaro et al. 2019). In particular, new discoveries about pulsating stars provided important input for asteroseismology, opening new frontiers and posing new questions. Some of those concern the classes of the A- and F-type pulsating variables located on or close to the main sequence, i.e. δ Scuti (δ Sct) and γ Doradus (γ Dor) stars.

The δ Sct stars generally exhibit pressure (p) modes that are excited by the κ mechanism in the He II ionization zone. They typically

oscillate with frequencies higher than ~ 5 d⁻¹. The δ Sct stars are mostly placed in the lower part of the classical instability strip. Recently, Murphy et al. (2019) classified a sample of over 15 000 *Kepler* A-type and F-type targets into δ Sct and non- δ Sct stars, also providing a subdivision in groups on the basis of the observed pulsation properties. They also defined a new empirical instability strip for δ Sct stars.

The γ Dor stars are a little cooler than the δ Sct variables. The gravity (g) mode oscillations of γ Dor stars are believed to be excited by the convective blocking mechanism (Guzik et al. 2000) with frequencies typically lower than 5 d⁻¹. In a recent study, it was suggested that the γ Dor-type pulsations are caused by the combination of κ mechanism and the convection–oscillation coupling (Xiong et al. 2016). The γ Dor domain partially overlaps the cool border of the theoretical instability strip of δ Sct stars. In this part, new variables called A–F-type hybrid stars were predicted

* E-mail: filizkahraman01@gmail.com (FKA); ennio.poretti@tng.iac.es (EP)

(Handler 1999; Dupret et al. 2004). These stars display both δ Sct- and γ Dor-type pulsations, i.e. p and g modes.

Before *Kepler*, only a few hybrid stars had been discovered by means of ground-based observations (Henry & Fekel 2005; Uytterhoeven et al. 2008; Handler 2009) and their positions in the Hertzsprung–Russell (H–R) diagram matched very well with the theoretically predicted region. The precision and near continuous nature of *Kepler* photometry revolutionized the field, showing that apparently there are many A–F-type hybrid stars located beyond the theoretical region (Grigahcène et al. 2010; Uytterhoeven et al. 2011). On the other hand, it was also found that some δ Sct and γ Dor stars are also placed outside the respective instability strips. These results give rise to conflicts with theory. Therefore, it was timely to fix the exact positions of these variables in the H–R diagram and to revise the borders of their instability strips. For these reasons, spectroscopic studies were carried out to determine accurate atmospheric parameters of δ Sct, γ Dor, and hybrid stars (e.g. Tkachenko et al. 2012; Niemczura et al. 2015, 2017). These investigations confirmed that some stars are actually outside the theoretical instability strips.

In particular, Balona (2014) and Balona et al. (2016) noticed how some gravity-mode pulsators are located close to, and even beyond, the hot border of δ Sct instability strip, defining them as hot γ Dor stars. These variables are remarkable objects because if the theory of convective driving would apply to stars located in this part of the H–R diagram, then they should not have a sufficient convective envelope to drive the γ Dor-type pulsations. It has been suggested that the hot γ Dor stars could be A- or B-type stars with a cooler γ Dor companion, or simply stars with wrong determinations of the effective temperature (T_{eff}). A spectroscopic study of hot γ Dor stars was undertaken (Balona et al. 2016) and it turned out that the resulting T_{eff} values were mostly consistent with those given in the *Kepler* input catalogue (KIC; Brown et al. 2011). However, the binary nature of the stars was not assessed and also the chemical composition of these variables could not be probed due to the low resolution of the spectra.

Another explanation is that the hot γ Dor stars are actually rapidly rotating slowly pulsating B (SPB) stars (Balona et al. 2016). Due to gravity darkening, their equatorial zones appear cooler than the rest of the surface, then they are classified as hot A-stars and, hence, as hot γ Dor variables. If this hypothesis is true, all hot γ Dor stars should rotate with high rotational velocities. There are also some hot hybrid stars that are located in the same area of the H–R diagram. In both cases, the γ Dor-type pulsation conflicts with the theory, since it would require that the convective blocking mechanism is continuing to be active in the hottest A stars (Balona 2014). The g-mode pulsation in those γ Dor stars can also be explained by the radiative κ mechanism and the coupling between oscillation and convection (Xiong et al. 2016).

In this study, a new spectroscopic survey of a selected sample of hot γ Dor and hybrid stars is presented. We focused on the candidate γ Dor and hybrid stars located close to the hot border of the δ Sct instability strip. We aim to answer the following questions. First, are the T_{eff} values of these hot objects correct? Secondly, do the hot γ Dor stars have hotter A- or B-type companions? Thirdly, are the hybrid stars members of binary or multiple systems? Can those hot variables be rapidly rotating stars? Additionally, are hot γ Dor and hybrid stars chemically peculiar? Therefore, we present a detailed spectroscopic analysis to determine the atmospheric parameters (T_{eff} , surface gravity $\log g$, and microturbulence velocity ξ), projected rotational velocities, binarity effects, and surface chemical abundances.

The target selection is described in Section 2. The spectroscopic observations, data reduction, and normalization are described in Section 3. The determinations of the atmospheric parameters from photometric indices, spectral energy distribution, and the analysis of Balmer and metal lines are discussed in Section 4. The chemical abundance analysis is presented in Section 5. The frequency analysis of the targets is performed in Section 6. The discussion and conclusions are given in Sections 7 and 8, respectively.

2 TARGET SELECTION

We started the selection process from the γ Dor and hybrid star candidates listed in the study of Uytterhoeven et al. (2011). They were proposed on the basis of their *Kepler* light curves and preliminary atmospheric parameters listed in the KIC. To better characterize them, we used the improved parameters reported in the revised *Kepler* catalogue of Huber et al. (2014, hereafter H14), the latest available at the time of our observations (October 2016). This catalogue is based on a compilation of literature values for atmospheric properties derived from a variety of observational techniques.

High-resolution spectroscopy of a well-constrained sample of stars should provide reliable answers to the questions posed in Section 1, especially when combining this technique with a homogeneous reduction and analysis of the spectra taken with a single instrument.

To refine our selection, we considered that the γ Dor stars have T_{eff} values in the range 6900 – 7300 K (Van Reeth et al. 2015) and that the hybrid stars are expected to be found at the intersection of the γ Dor and δ Sct instability strips, where T_{eff} changes approximately from 6600 to 7300 K. Given that the typical T_{eff} uncertainty is ~ 300 K (Niemczura et al. 2017) and hot γ Dor stars definition by Balona et al. (2016), we selected γ Dor and hybrid candidates with $T_{\text{eff}} \geq 7500$ K.

In the end, our selection contained nine hot γ Dor and 15 hot hybrid candidate stars (Table 1), for which high-resolution spectroscopy was not available. Some of them were observed with low-resolution spectroscopy (Balona et al. 2016; Frasca et al. 2016), but it is not possible to obtain reliable $\log g$ and metallicity values from this technique.

The positions of the targets in the $\log T_{\text{eff}} - \log g$ diagram are shown in Fig. 1. As can be seen from the figure, all stars are located beyond the blue edge of γ Dor instability strip. The T_{eff} values of the selected targets were also checked by using the updated parameters of the stars (Mathur et al. 2017, hereafter M17). It turned out that all targets except KIC 11508397 (~ 400 K cooler) still have T_{eff} values in the same range of the selection criteria. We used the M17 parameters in the following investigations.

3 SPECTROSCOPIC OBSERVATIONS

The stars were observed with the Fibre-fed Échelle Spectrograph (FIES), a cross-dispersed spectrograph mounted on the 2.56-m *Nordic Optical Telescope* of the Roque de los Muchachos Observatory in La Palma (Telting et al. 2014). The spectrograph offers three resolving power options. The maximum resolving power is $R = 67\,000$, while the medium- and low-resolving powers are $R = 46\,000$ and $R = 25\,000$, respectively, covering the wavelength range of 3700–8300 Å.

Since we aimed to derive atmospheric parameters and chemical abundances of the targets, we opted for the medium-resolution ($R = 46\,000$) configuration, taking into account the average

Table 1. Log of the observations (from 2016 October 13 to 19): number of the star (N_i) used in the paper, KIC ID, V-magnitude, signal-to-noise ratio (S/N), number of taken spectra (N_s), and input classification (Uytterhoeven et al. 2011).

N_i	KIC	V [mag]	S/N	N_s	Input classification
1	2168333	10.02	90	2	Hybrid
2	3119604	10.90	50	1	Hybrid
3	3231406	10.38	85	2	Hybrid
4	3240556	10.10	75	2	Hybrid
5	3245420	10.52	75	2	Hybrid
6	3868032	10.44	70	2	γ Dor
7	4677684	10.19	85	2	γ Dor
8	4768677	10.91	60	2	Hybrid
9	5180796	10.11	85	2	γ Dor
10	5630362	10.69	70	2	γ Dor
11	6199731	10.94	50	1	Hybrid
12	6500578	10.77	80	2	γ Dor
13	6776331	10.71	50	1	Hybrid
14	7694191	10.94	45	1	γ Dor
15	7732458	10.85	75	2	Hybrid
16	9052363	10.64	60	2	Hybrid
17	9775385	11.05	45	1	Hybrid
18	10281360	11.06	50	1	γ Dor
19	11197934	10.81	60	2	Hybrid
20	11199412	10.90	50	1	γ Dor
21	11508397	10.65	80	2	Hybrid
22	11612274	10.44	85	4	γ Dor
23	11718839	10.73	60	2	Hybrid
24	11822666	10.69	70	2	Hybrid

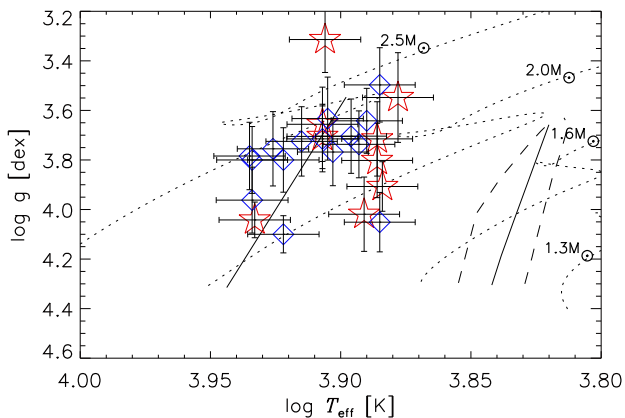


Figure 1. The positions of the selected candidate γ Dor (star symbols) and hybrid (diamonds) stars. The parameters of the stars were taken from Huber et al. (2014). The theoretical instability strips of the γ Dor (dashed lines) and δ Sct (solid lines) stars were taken from Dupret et al. (2005). The evolutionary tracks ($Z = 0.02$) were adopted from Kahraman Aliçavuş et al. (2016).

brightness of the sample ($V = 10.6$ mag). Observations were performed in the first halves of the nights from 2016 October 13 to 19. To examine the binarity nature of the targets, we tried to take at least two spectra per star on different nights. For some stars, only one spectrum could be taken due to the weather conditions and the limited observing time. The number of the spectra for each star and the signal-to-noise (S/N) ratios at around 5500 Å for combined spectra are given in Table 1.

The spectra were reduced by the dedicated pipeline FIESTool (Telting et al. 2014). The standard reduction procedure was applied.

Bias subtraction, correction of flat-field, scattered light extraction, wavelength calibration, and merging of orders were performed for each spectrum. Normalization of the reduced spectra was carried out manually by using the *continuum* task of the NOAO/IRAF package.¹

4 DETERMINATION OF THE ATMOSPHERIC PARAMETERS

The spectroscopic atmospheric parameters (T_{eff} , $\log g$, and ξ) were determined using the Balmer and iron lines, as done in previous several studies (e.g. Nieva & Przybilla 2010; Tkachenko et al. 2012; Niemczura et al. 2017). The approach we used in the analysis of the Balmer lines has been successfully applied in other papers (Catanzaro et al. 2011; Catanzaro & Balona 2012; Catanzaro, Ripepi & Bruntt 2013). In practice, the procedure minimized the difference between observed and synthetic spectra, using the χ^2 as goodness-of-fit parameter. Since the rotational velocity affects the profile of the lines, we determined initial estimates of projected rotational velocity ($v \sin i$) values by using the least-squares deconvolution technique (Donati et al. 1997). The $v \sin i$ values were measured from the zero positions of the Fourier transform of the mean line profiles (Table A1).

Synthetic spectra were generated in three steps. First, we computed local thermodynamic equilibrium atmospheric models using the ATLAS9 code (Kurucz 1993a, b). Secondly, the stellar spectra were then synthesized using SYNTHE (Kurucz & Avrett 1981). Thirdly, the spectra were convolved with the instrumental and rotational broadenings.

T_{eff} was estimated by computing the ATLAS9 model atmosphere, which gave the best match between the observed H_α , H_β , H_γ , and H_δ lines profile and those computed with SYNTHE. The models were computed using solar opacity distribution functions. It is also known that Balmer lines are not sensitive to $\log g$ parameter for $T_{\text{eff}} \lesssim 8000$ K (Smalley et al. 2002). Considering the T_{eff} range of our targets and the error bars, we fixed the $\log g$ and metallicity values to 4.0 dex and solar, respectively.

The Balmer lines are located far from the edges of the Echelle orders. The simultaneous fitting of four lines led to a final solution at the intersection of the four χ^2 iso-surfaces. An important source of uncertainty arose from difficulties in the normalization since it is always challenging for Balmer lines in Echelle spectra. The uncertainties on the T_{eff} values were estimated by introducing a 1σ change in the normalization level and a 0.2 dex error on $\log g$ and metallicity. We also considered the errors on the initial $v \sin i$ values (Table A1). These uncertainties were summed in quadrature with the errors obtained by the fitting procedure. The final results for T_{eff} values and their errors are reported in Table 2.

Final atmospheric parameters were derived by using the excitation and the ionization potentials of metal lines. For the correct atmospheric parameters of a star, all lines of the same element should give the same chemical abundance. The relationship between the chemical abundance and the excitation, ionization potentials of the same element should be flat.

We used Fe lines in the analysis, since they are the most numerous lines in the spectra having the T_{eff} range of our stars. The ATLAS9 (Kurucz 1993a, b) model atmospheres were synthesized by using the SYNTHE code (Kurucz & Avrett 1981) in this and the following chemical abundance analysis. A synthetic spectrum

¹<http://iraf.noao.edu/>

Table 2. The atmospheric parameters taken from M17 and our T_{eff} values derived from the analysis of Balmer lines. $E(B - V)$ values (Section 7.6) are also listed.

Number	KIC	$E(B - V)$ (mag) ± 0.02	$T_{\text{eff}M17}$ (K)	$\log g_{M17}$ (dex)	T_{eff} H lines (K)
1	2168333	0.03	8363^{+197}_{-395}	$3.80^{+0.36}_{-0.15}$	8000 ± 300
2	3119604	0.03	8383^{+233}_{-350}	$4.10^{+0.14}_{-0.15}$	7900 ± 360
3	3231406	0.02	8005^{+222}_{-333}	$3.77^{+0.40}_{-0.07}$	7600 ± 270
4	3240556	0.03	8615^{+238}_{-374}	$3.78^{+0.41}_{-0.14}$	8000 ± 300
5	3245420	0.11	8079^{+225}_{-338}	$3.72^{+0.43}_{-0.11}$	7900 ± 320
6	3868032	0.10	8564^{+234}_{-402}	$4.04^{+0.16}_{-0.16}$	8300 ± 610
7	4677684	0.22	8602^{+68}_{-94}	$3.78^{+0.28}_{-0.11}$	8600 ± 480
8	4768677	0.20	8584^{+77}_{-86}	$3.76^{+0.26}_{-0.03}$	8800 ± 830
9	5180796	0.15	8076^{+64}_{-96}	$3.82^{+0.22}_{-0.09}$	8100 ± 280
10	5630362	0.11	7821^{+78}_{-78}	$3.88^{+0.17}_{-0.07}$	7700 ± 170
11	6199731	0.05	8040^{+251}_{-306}	$3.64^{+0.55}_{-0.09}$	7500 ± 320
12	6500578	0.28	8072^{+223}_{-363}	$3.72^{+0.42}_{-0.10}$	8200 ± 450
13	6776331	0.08	7870^{+244}_{-325}	$3.70^{+0.46}_{-0.08}$	7600 ± 400
14	7694191	0.19	8070^{+251}_{-334}	$3.66^{+0.50}_{-0.09}$	8300 ± 580
15	7732458	0.02	7766^{+216}_{-324}	$3.64^{+0.49}_{-0.09}$	7300 ± 230
16	9052363	0.11	7810^{+216}_{-324}	$3.74^{+0.42}_{-0.10}$	7800 ± 360
17	9775385	0.05	7675^{+211}_{-316}	$4.05^{+0.17}_{-0.15}$	7300 ± 300
18	10281360	0.06	7776^{+216}_{-325}	$4.02^{+0.22}_{-0.14}$	7200 ± 280
19	11197934	0.06	7641^{+68}_{-91}	$3.83^{+0.22}_{-0.06}$	7600 ± 360
20	11199412	0.02	7693^{+239}_{-319}	$3.72^{+0.46}_{-0.08}$	7200 ± 280
21	11508397	0.00	7287^{+76}_{-87}	$3.87^{+0.18}_{-0.10}$	7200 ± 240
22	11612274	0.00	7694^{+214}_{-322}	$3.60^{+0.54}_{-0.06}$	7000 ± 190
23	11718839	0.03	8443^{+233}_{-367}	$3.76^{+0.42}_{-0.14}$	8100 ± 500
24	11822666	0.03	8615^{+238}_{-374}	$3.78^{+0.42}_{-0.14}$	8200 ± 540

is adjusted until it fits well the observed spectrum looking at χ^2 parameter (for more details, see Niemczura et al. 2015, Kahraman Aliçavuş et al. 2016). The Fe lines of all stars were analysed for a range of T_{eff} , $\log g$, and ξ with a step of 100 K, 0.1 dex, and 0.1 km s^{-1} , respectively. The range of the atmospheric parameters was selected taking into account the initial T_{eff} values derived from Balmer lines and the values given by M17 (Table 2). After the analysis was performed, we determined T_{eff} and $\log g$ values considering the excitation potential–abundance and the ionization potential–abundance relations, respectively. The ξ values were also obtained by checking the dependence between abundance and line strength. The obtained atmospheric parameters are given in Table 3. The uncertainties in the parameters were estimated by checking how much the parameters change for ~ 5 per cent differences in the excitation potential–abundance, ionization potential–abundance, and the abundance–line strength relationships.

The distributions of the derived atmospheric parameters are shown in Fig. 2. The final T_{eff} , $\log g$, and ξ ranges were obtained to be 7200–8600 K, 3.5–4.4 dex, and 1.5–4.4 km s^{-1} , respectively. The final atmospheric parameters were compared with the M17 atmospheric parameters. In most cases, T_{eff} values are consistent with each other within errors. However, in Fig. 3, the final $\log g$ values were also compared with the $\log g$ values given by M17. The final $\log g$ values are generally higher than the M17 $\log g$ values for the T_{eff} ranges of our stars. Additionally, it appears that the $\log g$ difference between our spectroscopic values and M17 ones

increases with the growing $\log g$. The relationship between those parameters is shown in the lower panel of Fig. 3.

Relations between ξ and T_{eff} and $\log g$ were checked as shown in Fig. 4. The $\xi - T_{\text{eff}}$ relationship has already been examined in several studies (e.g. Landstreet et al. 2009; Gebran et al. 2014; Niemczura et al. 2017). According to these studies, a decline in ξ is expected for the T_{eff} value higher than about 7000 K. The $\xi - \log g$ relationship was also examined by Gray, Graham & Hoyt (2001). They showed a relation between these two parameters for spectral types from A5 to G2. According to this relation, the ξ values decrease with increasing $\log g$. However, as our sample spans a T_{eff} range narrower than the A5–G2 one, we could not verify these relationships (Fig. 4).

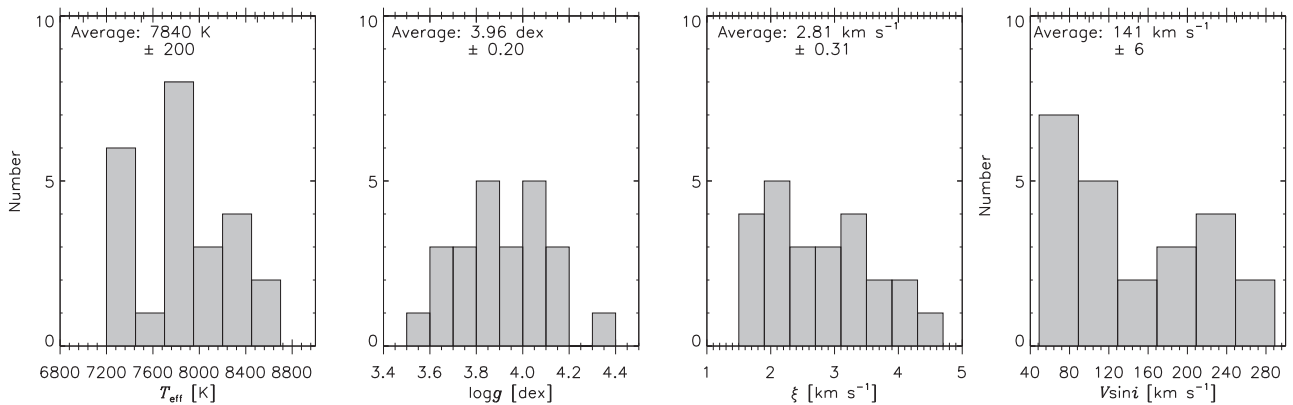
5 ANALYSIS OF CHEMICAL ABUNDANCES

Chemical abundances of the stars were derived by performing spectrum synthesis. The derived atmospheric parameters were taken as input during the analysis and the chemical abundances of individual elements were determined in addition to $v \sin i$.

In the first step of the analysis, all lines in the spectra were divided into subsets line by line. In the case of rapidly rotating stars, lines are mostly blended. Therefore, for rapidly rotating stars wider ranges in wavelength were selected considering the normalization level. For each subset, the line identifications were done by using the line list

Table 3. The final atmospheric parameters derived from the iron lines analysis, the $v \sin i$ values and the Fe abundances. The final pulsation-type classification is given in the last column as a result of our frequency analysis.

Number	KIC	T_{eff} (K)	$\log g$ (dex)	ξ (km s^{-1})	$\log \epsilon$ (Fe) (dex)	$v \sin i$ (km s^{-1})	Pulsation type
1	2168333	8400 \pm 200	3.7 \pm 0.2	2.0 \pm 0.5	7.47 \pm 0.27	175 \pm 9	δ Sct
2	3119604	7700 \pm 200	3.9 \pm 0.3	2.9 \pm 0.2	7.23 \pm 0.34	92 \pm 5	δ Sct
3	3231406	7900 \pm 100	3.8 \pm 0.2	2.1 \pm 0.2	7.63 \pm 0.31	169 \pm 10	Hybrid
4	3240556	7800 \pm 200	4.4 \pm 0.2	1.5 \pm 0.5	7.51 \pm 0.35	213 \pm 9	δ Sct
5	3245420	8100 \pm 200	3.7 \pm 0.1	2.0 \pm 0.2	7.58 \pm 0.32	151 \pm 6	δ Sct
6	3868032	8400 \pm 200	4.0 \pm 0.3	3.5 \pm 0.4	7.11 \pm 0.32	181 \pm 9	Non-pulsator
7	4677684	8500 \pm 200	3.5 \pm 0.2	1.7 \pm 0.3	7.52 \pm 0.28	71 \pm 3	γ Dor
8	4768677	8600 \pm 300	4.2 \pm 0.3	2.0 \pm 0.5	6.94 \pm 0.50	256 \pm 14	δ Sct
9	5180796	8400 \pm 200	4.0 \pm 0.2	2.5 \pm 0.2	7.73 \pm 0.30	152 \pm 6	γ Dor
10	5630362	7700 \pm 300	3.7 \pm 0.3	3.0 \pm 0.5	7.34 \pm 0.33	230 \pm 12	γ Dor
11	6199731	7800 \pm 200	4.1 \pm 0.3	4.4 \pm 0.4	7.23 \pm 0.35	236 \pm 10	δ Sct
12	6500578	7700 \pm 300	3.8 \pm 0.2	1.9 \pm 0.3	7.35 \pm 0.30	95 \pm 6	γ Dor
13	6776331	7900 \pm 200	3.9 \pm 0.1	2.3 \pm 0.2	7.65 \pm 0.32	49 \pm 3	Hybrid
14	7694191	8400 \pm 200	4.1 \pm 0.2	3.9 \pm 0.2	7.31 \pm 0.36	76 \pm 6	γ Dor
15	7732458	7800 \pm 200	4.1 \pm 0.2	2.6 \pm 0.2	7.73 \pm 0.34	87 \pm 5	δ Sct
16	9052363	8000 \pm 200	4.1 \pm 0.2	3.5 \pm 0.3	7.40 \pm 0.33	109 \pm 5	Non-pulsator
17	9775385	7400 \pm 200	4.2 \pm 0.2	4.1 \pm 0.2	7.44 \pm 0.36	71 \pm 3	Hybrid
18	10281360	7200 \pm 200	4.2 \pm 0.2	4.1 \pm 0.3	7.29 \pm 0.36	108 \pm 5	γ Dor
19	11197934	7600 \pm 200	3.9 \pm 0.2	3.0 \pm 0.5	7.46 \pm 0.31	267 \pm 18	Hybrid
20	11199412	7200 \pm 200	4.1 \pm 0.2	3.9 \pm 0.3	6.68 \pm 0.35	77 \pm 6	γ Dor
21	11508397	7200 \pm 200	3.9 \pm 0.3	1.5 \pm 0.5	7.68 \pm 0.30	240 \pm 11	Hybrid
22	11612274	7400 \pm 200	3.8 \pm 0.1	3.2 \pm 0.2	7.38 \pm 0.27	130 \pm 7	γ Dor
23	11718839	8100 \pm 200	3.9 \pm 0.1	3.4 \pm 0.2	7.45 \pm 0.32	57 \pm 3	δ Sct
24	11822666	8200 \pm 200	4.0 \pm 0.1	2.5 \pm 0.2	7.37 \pm 0.31	115 \pm 7	Hybrid

**Figure 2.** Distributions of the final atmospheric parameters determined from the iron lines analysis and $v \sin i$ values.

of Kurucz.² Then, these spectral subsets were analysed separately. The identified elements in each spectral subset and $v \sin i$ values were adjusted during the analysis. Taking the minimum difference between the observed and theoretical spectra, chemical abundances and $v \sin i$ values were obtained from each spectral subset. The range of $v \sin i$ was found to be from 49 to 267 km s^{-1} (Table 3, Fig. 2).

The average values of the abundances of individual elements for each star are given in Table A2 and the uncertainties given in this table are the standard deviations. The total uncertainties were estimated by considering the errors in the obtained atmospheric parameters, assumptions in the model atmospheres, the resolution, and the S/N ratio of spectra (Kahraman Aliçavuş et al. 2016). As a result, the uncertainty in the obtained abundances was found to be

0.28 dex on average. The total uncertainties were estimated for the Fe abundances (Table 3).

Consequently, we found that all stars have chemical abundances similar to solar (Asplund et al. 2009). There are three stars, KIC 3868032, KIC 4768677, and KIC 11199412, which seem to have moderately underabundant Fe ($[\text{Fe}/\text{H}] \lesssim -0.50$ dex). However, when the uncertainties in Fe abundances of these stars were considered, we can say that only KIC 11199412 has slightly lower Fe abundance. Additionally, this star displays underabundance in almost all elements compared to the solar abundances (Fig. 5). We compared our $[\text{Fe}/\text{H}]$ values and the values given by M17 (Fig. 6). According to the right-hand panel, the difference between the spectroscopic $[\text{Fe}/\text{H}]$ and the $[\text{Fe}/\text{H}]$ values given by M17 increases after $[\text{Fe}/\text{H}] = 0.0$ dex. However, the Spearman's rank coefficient R does not support the significance of such a trend: the correlation

²kurucz.harvard.edu/linelists.html

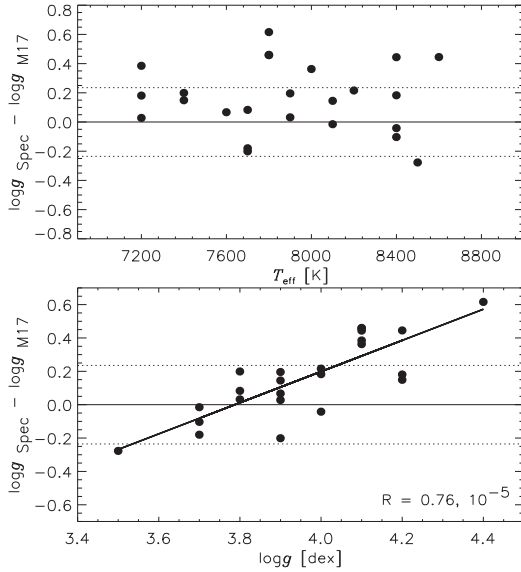


Figure 3. Differences between the final spectroscopic $\log g$ and the $\log g$ taken from M17 as a function of the final spectroscopic T_{eff} (upper panel) and $\log g$ (lower panel) obtained from the iron line analysis. Dashed lines represent $1\text{-}\sigma$ levels. The Spearman's rank correlation coefficient (R) and probability (the number after comma) are given in the right corner of the right-hand panel.

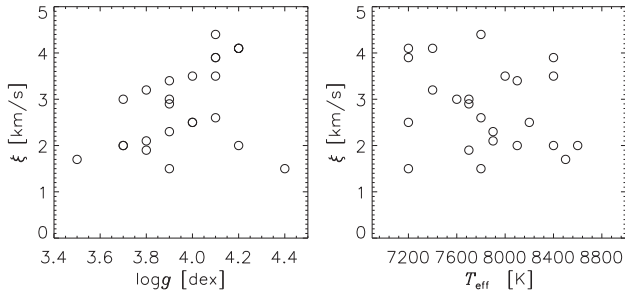


Figure 4. The final ξ as a function of the final spectroscopic T_{eff} (right-hand panel) and $\log g$ (left-hand panel).

coefficient of $R = 0.22$ and a probability value 0.31 indicate that there is no significant correlation.

Finally, KIC 11199412 clearly shows weak metal and Ca II K lines. KIC 11718839 also exhibits slightly weaker metal and Ca II K lines comparing the hydrogen spectral type but not enough to classify it as a peculiar star. For the sake of completeness, we report our final supervised spectral classification in Table A1.

6 FREQUENCY ANALYSIS OF PHOTOMETRIC DATA

To precisely classify the pulsational behaviour of the selected targets, we performed an independent frequency analysis of the *Kepler* data. The original time series were retrieved from the *MAST* archive.³ Keeping the subdivision into long- and short-cadence acquisition mode, the original data were normalized to the mean values of each quarter, thus correcting instrumental drifts. During this procedure, isolated outliers were removed. When reconstructing

³<http://archive.stsci.edu/>

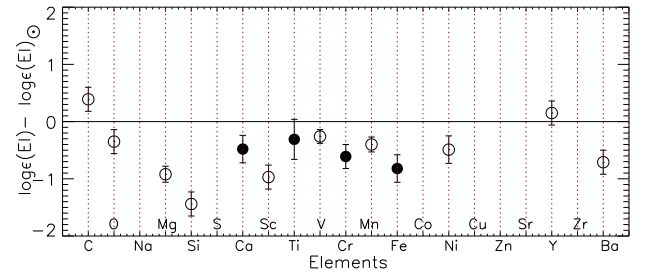


Figure 5. Differences between the derived chemical abundances and the solar values (Asplund et al. 2009) as a function of elements for KIC 11199412. Filled circles show the differences that were obtained from at least five and more lines, while others represent the opposite.

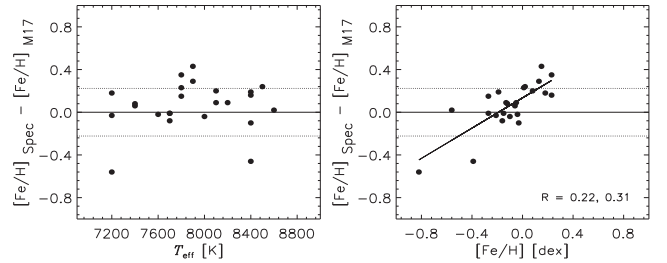


Figure 6. Differences between the spectroscopic $[\text{Fe}/\text{H}]$ and $[\text{Fe}/\text{H}]$ taken from H14 as a function of the spectroscopic $[\text{Fe}/\text{H}]$ (left-hand panel) and T_{eff} (right-hand panel). The Spearman's rank correlation coefficient (R) and probability (the number after comma) are given in the right corner of the right-hand panel.

the pulsational content of our variables, we used the short-cadence time series to investigate the region above the Nyquist frequency ($f = 24.5 \text{ d}^{-1}$) of the more numerous long-cadence data.

The accurate time series were then analysed for their constituent frequencies with the goal to establish their modal content. We have used the iterative both sine-wave fitting method (Vaniček 1971) and the software package Period04 (Lenz & Breger 2005). The final goal is to determine the pulsational characteristics with respect to the spectroscopic properties and the position in the H–R diagram. The initial variability classification of our targets (γ Dor, hybrid) was taken from Uytterhoeven et al. (2011). When our analysis was almost finished, Murphy et al. (2019) used *Gaia*-derived luminosities to propose another classification scheme based on the skewness of the amplitudes in the Fourier spectra. However, these authors focused on the δ Sct stars, without investigating the frequency region below 5 d^{-1} , where γ Dor and hybrid stars are expected to show their g modes.

6.1 Variability not induced by pulsation

The most obvious case was that of KIC 3868032. The frequency spectrum clearly shows peaks at $f = 0.40 \text{ d}^{-1}$, $2f$, $3f$, and $4f$. The spectroscopic analysis pointed out a mean profile with two superimposed components, with clearly different rotational regimes, i.e. $v \sin i = 180 \text{ km s}^{-1}$ and $v \sin i < 100 \text{ km s}^{-1}$. Uytterhoeven et al. (2011) classified it as a γ Dor variable. However, these peaks are associated with the orbital motion and cannot be ascribed to pulsation. We noticed that after considering f and harmonics, a peak at $f_1 = 1.68 \text{ d}^{-1}$ appears close but not equal to $4f$. It could be still an artefact of the orbital/rotational effects but its pulsational origin cannot be ruled out.

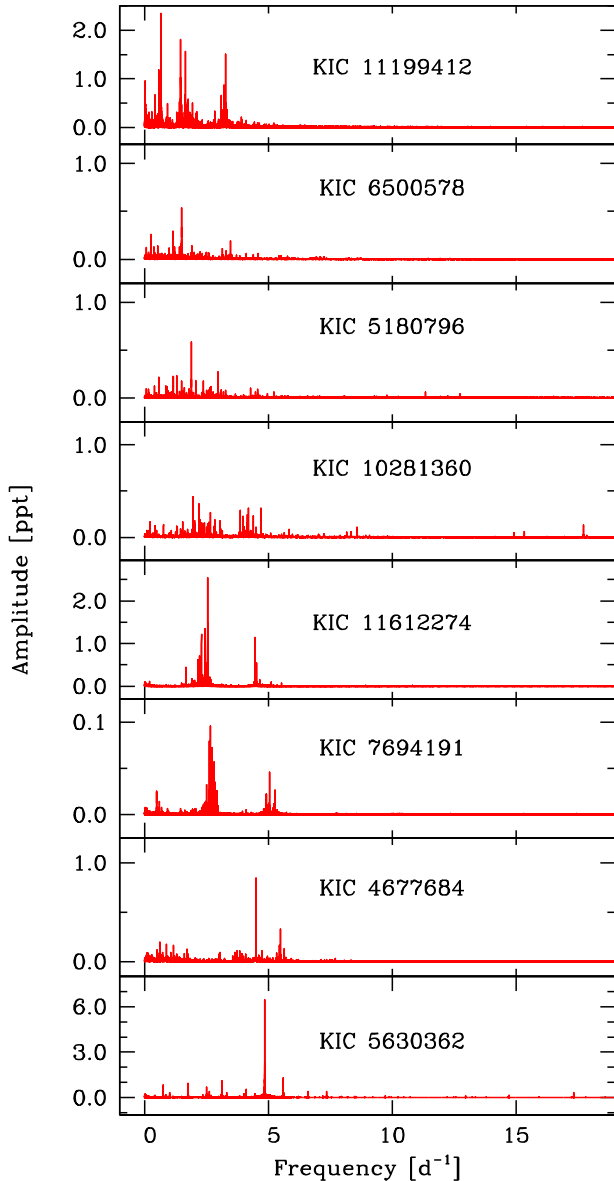


Figure 7. Amplitude spectra obtained by combining short- and long-cadence data of the variables showing a regime of low-frequency ($f \leq 6 \text{ d}^{-1}$) modes. They are ordered for increasing frequency of the highest peak.

The case of KIC 9052363 is similar. The light curve is almost flat, without any clear feature that could be ascribed to pulsation. The frequency analysis reveals a couple of low-frequency, very-low amplitude peaks. Due to their incoherence, small rotational effects are the most plausible reason. Both stars are also reported as non- δ Sct by Murphy et al. (2019).

6.2 Low-frequency regime

Eight stars in our sample show a set of low-frequency peaks only. We ordered them by increasing frequency of the strongest peak (Fig. 7). We note that the range of frequencies is small, not exceeding 6 d^{-1} . Occasional high-frequency peaks appear in the frequency spectra not enough to claim that a clear double regime of pulsation is present. It is noteworthy that all stars in Fig. 7 were classified as γ Dor by Uytterhoeven et al. (2011). Actually, they are the only

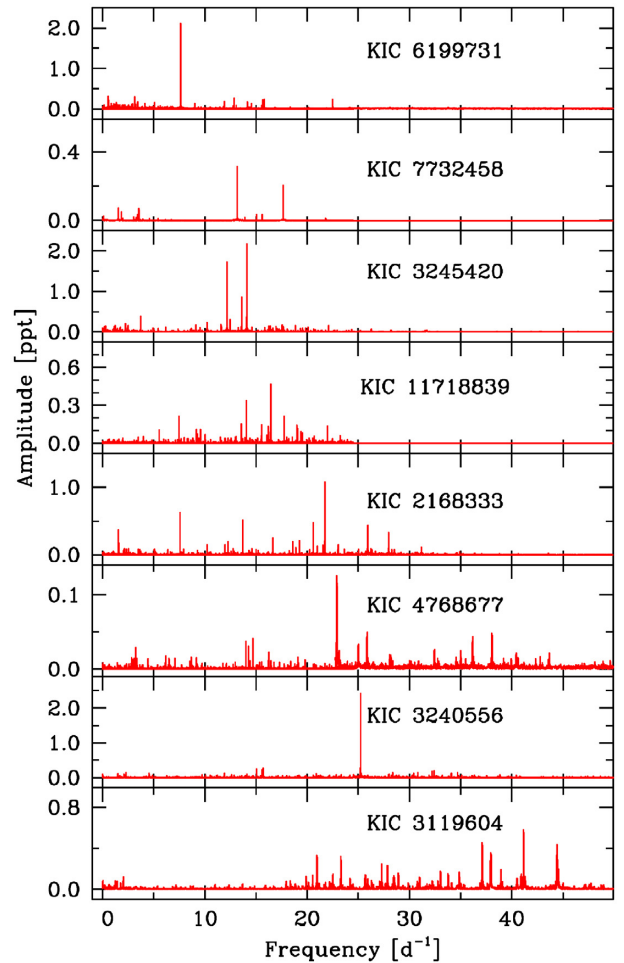


Figure 8. Amplitude spectra obtained by combining short- and long-cadence data of the variables showing a prevailing regime of high-frequency modes. They are ordered for increasing frequency of the highest peak.

stars classified as γ Dor in our sample and therefore we are in full agreement.

KIC 5630362 is the star showing the highest frequency ($f = 4.856 \text{ d}^{-1}$, $P = 0.206 \text{ d}$), with an amplitude much larger than those of the others (bottom panel). It is unlikely that this frequency is that of the fundamental radial mode, since the long period would suggest an evolved δ Sct star: the very fast rotation (230 km s^{-1}) and the gravity ($\log g = 3.7 \text{ dex}$) do not support such a hypothesis. Therefore, pulsators with largely predominant modes also exist in γ Dor stars, not only in δ Sct ones (i.e. the Group A proposed by Murphy et al. 2019).

6.3 High-frequency regime

None of the stars in our sample was classified as a pure δ Sct star. However, our frequency analysis showed that some stars are characterized by a large set of high-frequency peaks accompanied by no (or a few) low-frequency ones (Fig. 8). The case of KIC 3240556 is noteworthy, since this star shows a largely predominant mode. The frequency is too high ($f = 25.2 \text{ d}^{-1}$) to be due to rotation. Note that the short-cadence time series allowed us to determine the exact value of this high frequency very close to the Nyquist frequency of the long-cadence data. KIC 3240556 surely belongs to Group A in the Murphy et al. (2019) classification scheme.

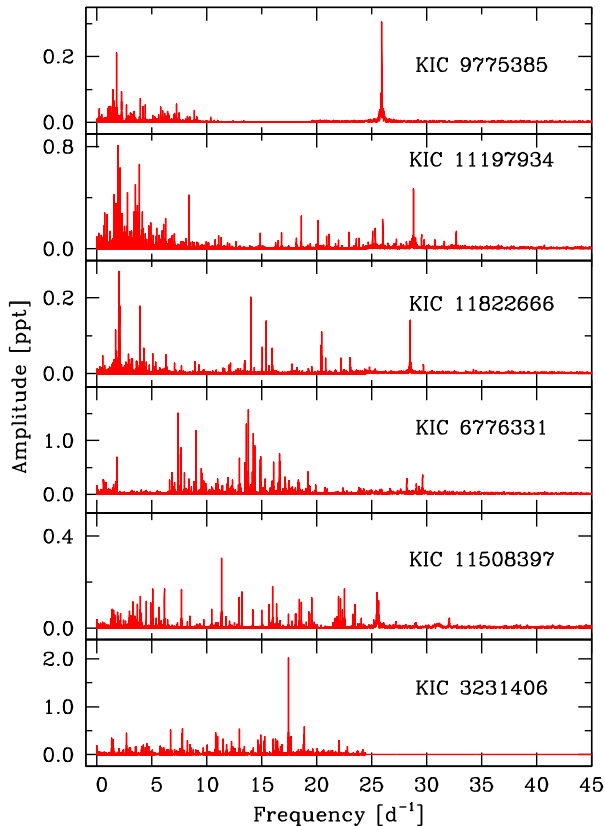


Figure 9. Amplitude spectra obtained by combining short- and long-cadence data of the variables showing clear regimes of both high-frequency and low-frequency peaks.

All these variables were classified as hybrid stars. However, we know from the analysis of line-profile variations that very high-degree modes (up to $\ell = 14$) are excited in δ Sct stars and they are spectroscopically detectable (Poretti et al. 2009; Mantegazza et al. 2012). The rotational splitting can shift the frequencies of retrograde modes of multiplets toward low values, thus producing the bunch of peaks observed there in hybrid stars. They also could be combination terms between high-frequency modes or again effects of the rotational modulation induced by changing spots and/or faculae on the stellar surfaces. We emphasize that in general this multiplicity of causes does not make a few low-frequency peaks on their own a sufficient criterion to claim for an hybrid pulsational regime.

6.4 Low- and high-frequency regime

Only six stars show simultaneously well-defined low- and high-frequency regimes (Fig. 9), with clear peaks in both regions. However, it has to be noted how the amplitude spectra differ: there are low and high frequencies both confined in separated groups and continuously distributed. All these stars had an input classification as hybrid variables.

7 DISCUSSION

We can now use the results from the frequency and atmospheric analyses to better define the properties of our targets and closely look at how much they are really peculiar, as suggested by previous

works. Our new classification and parameters are reported in Table 3. In the left-hand panel of Fig. 10, the $\log T_{\text{eff}} - \log g$ positions are shown on the basis of the predicted atmospheric parameters by M17, while in the right-hand panel, our final atmospheric parameters are used. As can be noticed, the larger changes in the positions are mostly due to the differences in the $\log g$ values.

7.1 Binary nature

Composite spectra suggesting double-lined spectroscopic binaries are not observed, except for the ellipsoidal variable KIC 3868032 (Section 6.1). Seventeen stars in our sample have at least two spectra taken on different nights. The radial velocities were examined: if there was a companion, the radial velocities should vary due to the orbital motion. We did not find any large variation in the radial velocities. Nevertheless, the very small number of observations and their very limited time coverage do not allow us to clearly detect long-period or small-amplitude or low-inclination binary systems. For example, KIC 2168333 and KIC 11508397 are known binaries with very long orbital periods ($\gtrsim 350$ d; Murphy et al. 2018), but the radial velocities obtained from their two spectra differ by 2.6 and 1.5 km s^{-1} only, respectively.

7.2 Pulsation characteristics versus new atmospheric parameters

Our detailed frequency analysis was able to clean the physical scenario since 10 targets (eight δ Sct and two non-pulsating stars; Sections 6.1 and 6.2, respectively) out of 24 (42 per cent) can be retired from the initial sample of γ Dor and hybrid pulsators. In particular, the 8 δ Sct stars erroneously classified as hybrid variables turned out to be normal p-mode pulsators, well inside the δ Sct instability strip. Additionally, the two non-pulsators remain located close to the hot border of the δ Sct domain, where the fraction of δ Sct pulsating stars is estimated to be ~ 40 per cent (Murphy et al. 2019).

Among the six hybrid variables, only KIC 11822666 is really a hot star (8200 K), while the T_{eff} of KIC 9775385, KIC 11197934, and KIC 11508397 are very close or below the 7300 K limit when taking into account the error bars. KIC 6776331 and KIC 3231406 have intermediate values (7900 K).

A similar count applies to the eight targets re-classified as pure γ Dor stars: five (KIC 5630362, KIC 6500578, KIC 10281360, KIC 11199412, and KIC 11612274) have T_{eff} values in agreement with that of the hot border of the classical γ Dor strip (assuming 1σ error bars), though KIC 5630362 and KIC 6500578 seem to be more luminous than usual for γ Dor stars. Note that the normal γ Dor pulsator KIC 11199412 is the only star showing hints of chemical peculiarities (Section 7.4). In three cases (KIC 4677684, KIC 7694191, and KIC 5180796), the T_{eff} values are well above 8000 K.

In the end, we have eight stars (three hybrid and five normal γ Dor pulsators) that show g modes even if they are beyond the hot border of the γ Dor instability strip: namely, KIC 3231406, KIC 6776331, KIC 11822666, KIC 4677684, KIC 5180796, KIC 5630362, KIC 6500578, and KIC 7694191. They constitute our final bona fide sample. We recall that the whole initial sample (24 stars) was expected to be composed of such unusual γ Dor pulsators.

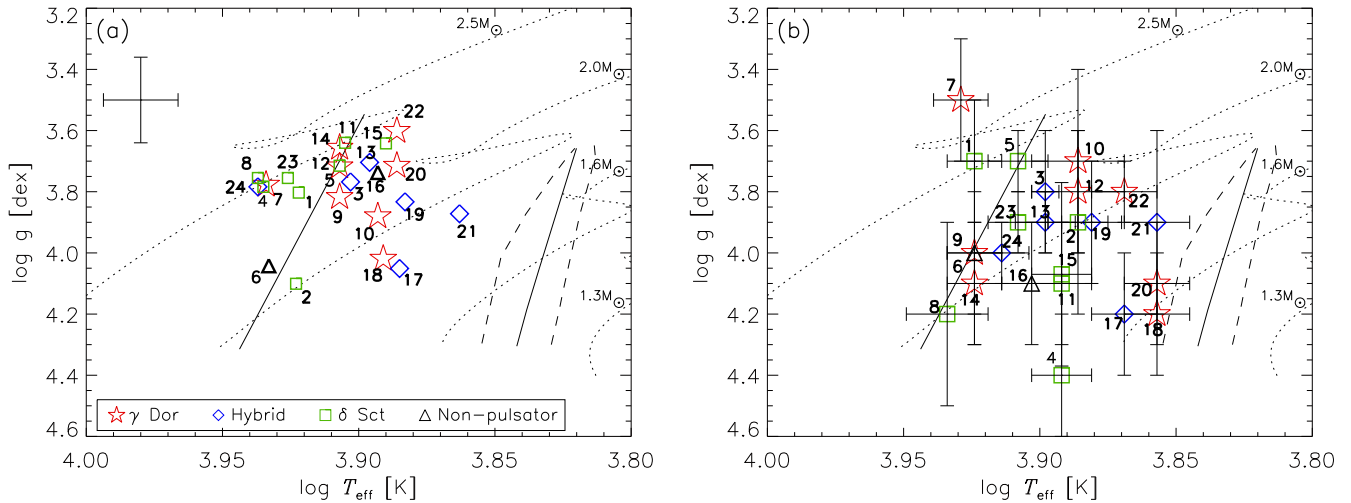


Figure 10. (a) The positions of the target stars, as numbered in Table 3, according to the atmospheric parameters given by M17. (b) The positions of the stars according to the final atmospheric parameters. The theoretical instability strips of the γ Dor (dashed lines) and δ Sct (solid lines) stars were taken from Dupret et al. (2005). The evolutionary tracks ($Z = 0.02$) were adopted from Kahraman Aliçavuş et al. (2016).

7.3 Other atmospheric parameters

When the obtained atmospheric parameters are taken into account, most stars are found that they have T_{eff} values in agreement with those given by M17. Only two stars, KIC 10281360 and KIC 11199412, show spectroscopic T_{eff} values about 500 K cooler than the previously given values by M17. This explains why the previous classification put them so close to the hot border.

Our final $\log g$ values were compared with the $\log g$ values given by M17 (Fig. 3). In some cases, the final $\log g$ values differ more than 0.4 dex. Therefore, the positions of these stars change in the $\log T_{\text{eff}} - \log g$ diagram (Fig. 10). When taking into account the final positions in the $\log T_{\text{eff}} - \log g$ diagram and the evolutionary tracks, we can say that ~ 70 per cent of stars have masses from 2.0 to 2.5 M_{\odot} , while the mass range of the others is between 1.6 and 2.0 M_{\odot} .

The microturbulent velocity ξ changes with T_{eff} (Gray et al. 2001; Smalley 2004; Landstreet et al. 2009) and the ξ value varies from ~ 1.5 to 3 km s^{-1} for T_{eff} range of about 7000–7300. However, three cool stars (KIC 9775385, KIC 10281360, and KIC 11199412) have ξ values between 3.9 and 4.1 km s^{-1} with a maximum uncertainty of 0.3 km s^{-1} . These ξ values are high for this T_{eff} range, but the three stars seem to be normally located on the cool border of the γ Dor instability strip. For the other hotter stars, the ξ range is between 1.5 and 4.5 (± 0.3) km s^{-1} , as expected for A-type stars.

Some target stars have low-resolution LAMOST spectroscopy in the literature. The atmospheric parameters derived from these studies are given in Table A3. When we compared these results with our final atmospheric parameters, we found significant differences and trends between the parameters obtained from the high- and low-resolution spectroscopy (Fig. 11). This will solve the problem.

7.4 Chemical abundances

Anomalous abundances, like the Am phenomenon (Hareter et al. 2011), have been considered a possible physical explanation of the hybrid γ Dor– δ Sct pulsation. Our analysis did not reveal any abundance peculiarity in our bona fide sample of eight hot γ Dor and hybrid stars, in agreement with recent studies showing that most hybrid stars are chemically normal (Niemczura et al. 2015, 2017). We also searched for He lines, without any significant detection.

Only KIC 11199412 (a normal γ Dor star) exhibits a moderate underabundance in almost all the elements (Fig. 5).

7.5 The $v \sin i$ values and the SPB hypothesis

It has been suggested that hot γ Dor stars are actually rapidly rotating SPB stars (Salmon et al. 2014; Balona et al. 2015). Due to gravity darkening, their equatorial zones appear cooler than the rest of the surface, then they are classified as hot A-stars and, hence, as hot γ Dor variables.

Balona et al. (2016) determined an average $v \sin i = 114 \text{ km s}^{-1}$ for a group of six hot γ Dor stars. Our five bona fide hot γ Dor stars show $v \sin i$ values ranging from 71 to 230 km s^{-1} (Table 3), with an average value of 125 km s^{-1} . In the spectral range B5–B9, main-sequence stars, like SPB variables, show a mean $v \sin i = 144 \text{ km s}^{-1}$ (Głębocki & Gnański 2005; Balona et al. 2016). Since hot γ Dor stars do not seem to rotate faster than normal SPB stars, they do not constitute a special SPB subclass. Moreover, we could not find spectral lines indicative of the B-type (Section 7.4), which should be present at least for SPB stars seen at intermediate or pole-on orientations. Finally, gravity darkening does not seem to be able to lower the T_{eff} of SPB stars sufficiently to approach the hot border of the δ Sct instability strip (see Fig. 4 in Salmon et al. 2014). We prudently note that the classification as hot or classical hybrid/ γ Dor stars could also be affected by the gravity darkening, especially in case of fast rotators seen almost equator-on, like KIC 5630362, KIC 11197934, and KIC 11508397.

7.6 Gaia parallaxes

As a final check, we used the *Gaia* parallaxes (Gaia Collaboration 2018) to investigate the positions of the stars in the H–R diagram. We adopted the bolometric corrections computed taking into account the T_{eff} values (Flower 1996). The extinction coefficients (A_V) were estimated using the interstellar reddening $E(B - V)$ values (Table 2). These were obtained by measuring the equivalent widths of the NaD lines in our spectra and then applying the relation given by Munari & Zwitter (1997).

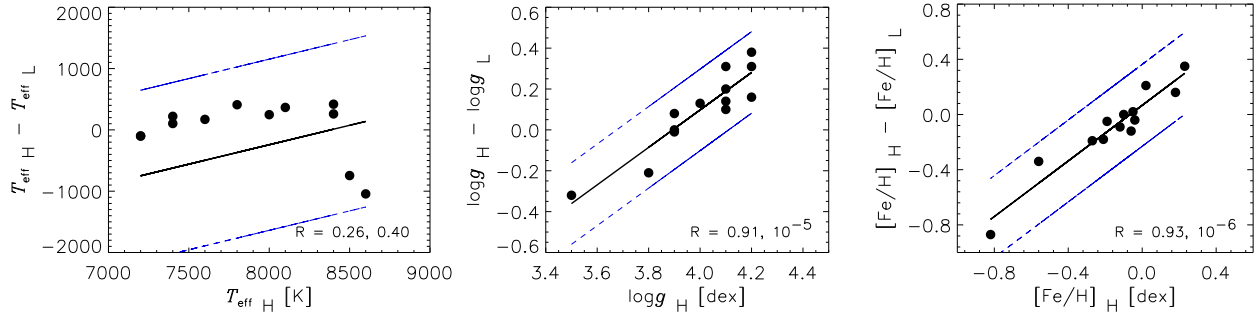


Figure 11. Comparison of the atmospheric parameters obtained from high- and low-resolution spectroscopy. The subscripts H and L define the high- and low-resolution spectroscopy, respectively. The Spearman's rank correlation coefficient (R) and probability (the number after comma) are given in the right corner of the panels. Blue lines represent the 1σ levels.

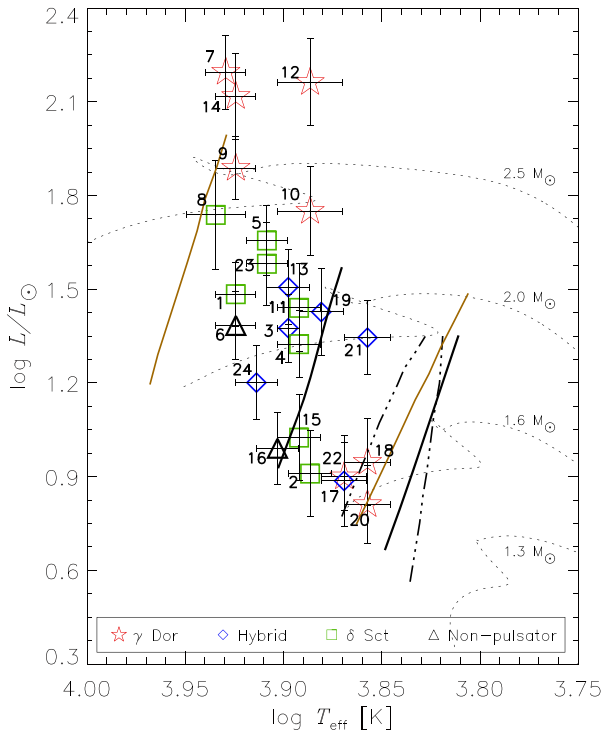


Figure 12. The positions of the stars in the H–R diagram, as numbered in Table 1. The theoretical instability strips of the γ Dor (dashed lines) and δ Sct (solid black lines) stars were taken from Dupret et al. (2005). The recently suggested δ Sct instability strip (Murphy et al. 2019) is shown by brown solid lines. The evolutionary tracks ($Z = 0.02$) were adopted from Kahraman Alıçavuş et al. (2016).

An offset of -0.03 mas in the *Gaia* parallaxes was found (Lindgren et al. 2018; Zinn et al. 2019). However, when this offset was applied to a large sample ($\sim 15\,000$ stars), a huge amount of stars goes below the zero-age main sequence with unreasonably low luminosities (Murphy et al. 2019). Therefore, to calculate our final *Gaia* luminosities, we did not apply this offset to the parallaxes, accordingly with recent studies (Arenou et al. 2018; Murphy et al. 2019). The positions of the stars in the H–R diagram are illustrated in Fig. 12. Note that the new empirical instability strip of δ Sct stars (Murphy et al. 2019) now incorporates some variables located beyond the hot border of the previous theoretical instability strip.

As can be noticed from Fig. 12, stars 7, 9, 10, 12, and 14 (see Table 3 for their KIC identification) have very high luminosities.

When the radii of those hot γ Dor stars were calculated using the *Gaia* luminosities, we obtained values ranging from 4.3 to 6.0 R_{\odot} . We also calculated the radii of the hot γ Dor stars classified by Balona et al. (2016). It turned out that ~ 70 per cent of their sample have larger radii ($3.2 < R_{\odot} < 7.2$). Main-sequence A–F-type stars should have radii in the range 1.5–2.7 R_{\odot} (Cox 2000). Therefore, the larger size of the hot γ Dor pulsators appears to support the hypothesis that they are different from main-sequence A–F pulsators. They could be evolved as A–F stars or more massive stars (such as B-type stars) entering the classical instability strip in their redward evolution. The impact of enhanced iron opacity on stellar pulsations can lead to a substantial revision of the instability strips (Moravveji 2016) and then play a key role to explain the location of our hot hybrid and γ Dor variables. Additionally, the higher luminosity values of these hot stars may be the result of binarity. These systems could be a member of a long orbital period binary system, which could not detect with our present spectroscopic data.

8 CONCLUSIONS

We performed a detailed spectroscopic and photometric study of a group of 24 *Kepler* targets, all claimed to be hot γ Dor or δ Sct- γ Dor hybrid stars, located well beyond the theoretical γ Dor instability strip (Uytterhoeven et al. 2011). The detailed frequency analysis of the *Kepler* time series and the determination of T_{eff} and other atmospheric parameters performed with the new FIES spectra allowed us to set the bona fide sample of such peculiar pulsators to five hot γ Dor stars and three hot hybrid stars. If on one hand we provide a strong confirmation that these peculiar pulsators exist, on the other we reduce their recurrence to one-third to what originally evaluated. Therefore, we can assume that the physical explanation should reside in a mechanism or a cause applicable to a limited number of stars, not to the vast majority of the δ Sct or γ Dor variables.

Searching for this still elusive explanation, we did not find any peculiarity in the atmospheric parameters and chemical abundances. The lack of composite spectra does not support the possibility that the hot hybrid stars are binaries in which one or both components are normal δ Sct and/or γ Dor pulsators. We investigated the rotation rate and we cannot support the hypothesis that hot γ Dor pulsators are actually fast-rotating SPB stars. On the other hand, *Gaia* luminosities suggested us that hot γ Dor pulsators have larger radii and higher luminosities than normal main-sequence A–F stars. New efforts, both theoretical and observational, have to be made to well constrain all the features of this new scenario.

ACKNOWLEDGEMENTS

The authors thank the anonymous referee for useful comments that have improved the presentation of their results. The authors also thank Simon Murphy for his useful comments on a first draft of the manuscript. This article is based on observations made with the *Nordic Optical Telescope*, operated by the Nordic Optical Telescope Scientific Association at the Observatorio del Roque de los Muchachos, La Palma, Spain, under the proposal 54-003 (P.I. E. Poretti). The authors thank the whole NOT staff for the help in the observations, performed in visitor mode. FKA and GH thank the Polish National Center for Science (NCN) for supporting the study through grant 2015/18/A/ST9/00578. EN acknowledges support provided by the Polish National Science Center through grant no. 2014/13/B/ST9/00902. This work has been partly supported by the Scientific and Technological Research Council of Turkey (TUBITAK) grant numbers 2214-A and 2211-C. The calculations have been carried out in Wrocław Centre for Networking and Supercomputing (<http://www.wcss.pl>), grant No. 214. This research has made use of the SIMBAD data base, operated at CDS (the Centre de Données astronomiques de Strasbourg Strasbourg), France.

REFERENCES

- Arenou F. et al., 2018, *A&A*, 616, A17
 Asplund M., Grevesse N., Sauval A. J., Scott P., 2009, *ARA&A*, 47, 481
 Balona L. A., 2014, *MNRAS*, 437, 1476
 Balona L. A., Baran A. S., Daszyńska-Daskiewicz J., De Cat P., 2015, *MNRAS*, 451, 1445
 Balona L. A. et al., 2016, *MNRAS*, 460, 1318
 Borucki W. J. et al., 2010, *Science*, 327, 977
 Brown T. M., Latham D. W., Everett M. E., Esquerdo G. A., 2011, *AJ*, 142, 112
 Catanzaro G., Balona L. A., 2012, *MNRAS*, 421, 1222
 Catanzaro G. et al., 2011, *MNRAS*, 411, 1167
 Catanzaro G., Ripepi V., Bruntt H., 2013, *MNRAS*, 431, 3258
 Compton D. L., Bedding T. R., Stello D., 2019, *MNRAS*, 485, 560
 Cox A. N., 2000, *Allen's Astrophysical Quantities*. AIP Press; Springer, New York
 Donati J.-F., Semel M., Carter B. D., Rees D. E., Collier Cameron A., 1997, *MNRAS*, 291, 658
 Dupret M.-A., Grigahcène A., Garrido R., Gabriel M., Scuflaire R., 2004, *A&A*, 414, L17
 Dupret M.-A., Grigahcène A., Garrido R., Gabriel M., Scuflaire R., 2005, *A&A*, 435, 927
 Flower P. J., 1996, *ApJ*, 469, 355
 Frasca A. et al., 2016, *A&A*, 594, A39
 Gaia Collaboration, 2018, *A&A*, 616, A1
 Gebran M., Monier R., Royer F., Lobel A., Blomme R., 2014, in Gautier M. et al., eds, *Putting A Stars into Context: Evolution, Environment, and Related Stars*, Proceedings of the International Conference, Russia, p. 193
 Głębocki M., Gnaçiński R., 2005, in Favata F., Hussain G. A. J., Battrick B., eds, *Proceedings of the 13th Cambridge Workshop on Cool Stars, Stellar Systems and the Sun*, 571, ESASP.560. European Space Agency, Hamburg, Germany
 Gray R. O., Graham P. W., Hoyt S. R., 2001, *AJ*, 121, 2159
 Grigahcène A. et al., 2010, *ApJ*, 713, L192
 Guzik J. A., Kaye A. B., Bradley P. A., Cox A. N., Neuforge C., 2000, *ApJ*, 542, L57
 Handler G., 1999, *MNRAS*, 309, L19
 Handler G., 2009, *MNRAS*, 398, 1339
 Hareter M., Fossati L., Weiss W., Suárez J. C., Uytterhoeven K., Rainer M., Poretti E., 2011, *ApJ*, 743, 153
 Helminiak K. G., Konacki M., Maehara H., Kambe E., Ukita N., Ratajczak M., Pigulski A., Kozłowski S. K., 2019, *MNRAS*, 484, 451
 Henry G. W., Fekel F. C., 2005, *AJ*, 129, 2026
 Huber D. et al., 2014, *ApJS*, 211, 2 (H14)
 Kahraman Aliçavuş F. et al., 2016, *MNRAS*, 458, 2307
 Koch D. G. et al., 2010, *ApJ*, 713, L79
 Kurucz R., 1993, *ATLAS9 Stellar Atmosphere Programs and 2 km/s grid*. Kurucz CD-ROM No. 13. Smithsonian Astrophysical Observatory, Cambridge, MA, p. 13
 Kurucz R. L., 1993, in Dworetzky M. M., Castelli F., Faraggiana R., eds, *ASP Conf. Ser. Vol. 44, Peculiar versus Normal Phenomena in A-type and Related Stars*, IAU Colloquium 138. Astron. Soc. Pac., San Francisco, p. 87
 Kurucz R. L., Avrett E. H., 1981, *Solar Spectrum Synthesis. I. A Sample Atlas from 224 to 300 nm*. SAO Special Report, p. 391
 Landstreet J. D., Kupka F., Ford H. A., Officer T., Sigut T. A. A., Silaj J., Strasser S., Townshend A., 2009, *A&A*, 503, 973
 Lenz P., Breger M., 2005, *CoAst*, 146, 53
 Lindegren L. et al., 2018, *A&A*, 616, A2
 Mantegazza L. et al., 2012, *A&A*, 542, A24
 Mathur S. et al., 2017, *ApJS*, 229, 30 (M17)
 Moravveji E., 2016, *MNRAS*, 455, L67
 Munari U., Zwitter T., 1997, *A&A*, 318, 269
 Murphy S. J., Moe M., Kurtz D. W., Bedding T. R., Shibahashi H., Boffin H. M. J., 2018, *MNRAS*, 474, 4322
 Murphy S. J., Hey D., Van Reeth T., Bedding T. R., 2019, *MNRAS*, 485, 2380
 Niemczura E. et al., 2015, *MNRAS*, 450, 2764
 Niemczura E. et al., 2017, *MNRAS*, 470, 2870
 Nieva M.-F., Przybilla N., 2010, *EAS*, 167, 43
 Pizzocaro D. et al., 2019, *A&A*, 628, A41
 Poretti E. et al., 2009, *A&A*, 506, 85
 Qian S.-B., Li L.-J., He J.-J., Zhang J., Zhu L.-Y., Han Z.-T., 2019, *RAA*, 19, 001
 Salmon S. J. A. J., Montalbán J., Reese D. R., Dupret M.-A., Eggenberger P., 2014, *A&A*, 569, A18
 Smalley B., 2004, *IAU Symp.*, 224, 131
 Smalley B., Gardiner R. B., Kupka F., Bessell M. S., 2002, *A&A*, 395, 601
 Telting J. H. et al., 2014, *AN*, 335, 41
 Tkachenko A., Lehmann H., Smalley B., Debusscher J., Aerts C., 2012, *MNRAS*, 422, 2960
 Uytterhoeven K. et al., 2008, *A&A*, 489, 1213
 Uytterhoeven K. et al., 2011, *A&A*, 534, AA125
 Van Reeth T. et al., 2015, *ApJS*, 218, 27
 Vaníček P., 1971, *Astrophys. Space Sci.*, 12, 10
 Xiong D. R., Deng L., Zhang C., Wang K., 2016, *MNRAS*, 457, 3163
 Zinn J. C., Pinsonneault M. H., Huber D., Stello D., 2019, *ApJ*, 878, 136

APPENDIX

Table A1. The initial $v \sin i$ values derived for the Balmer lines analysis (Section 4) and our spectral classification (Section 5).

KIC	$v \sin i$ (km s^{-1})	Spectral type
2168333	163 ± 15	kA5hA4 V
3119604	94 ± 1	A5 V
3231406	173 ± 6	A7 III–IV
3240556	218 ± 4	A5 IV–V
3245420	158 ± 4	A7 V
3868032	178 ± 4	A5 V
4677684	75 ± 5	A3 IV–V
4768677	257 ± 14	A3 IV–V
5180796	155 ± 3	A4 IV–V
5630362	242 ± 12	A5 III–IV
6199731	241 ± 3	A5 III
6500578	98 ± 3	A3 IV
6776331	51 ± 1	A7 V
7694191	78 ± 1	A5 IV–V
7732458	82 ± 2	A9 IV–V
9052363	109 ± 2	A5 IV–V
9775385	72 ± 1	F0 V
10281360	111 ± 4	A9 IV–V
11197934	295 ± 5	A8 IV–V
11199412	73 ± 2	kA3hF0mA3 V
11508397	245 ± 6	F0 V
11612274	132 ± 4	F0 V
11718839	57 ± 4	kA7hA5mA7 V, kA6hA5mA6 V
11822666	121 ± 4	A5 V

Table A2. Average abundances and standard deviations of individual elements. Number of the analysed spectral parts is given in the brackets.

Atomic number	Elements	KIC 2168333	KIC 3119604	KIC 3231406	KIC 3240556	KIC 3245420
6	C	8.45 ± 0.18 (1)	8.54 ± 0.19 (4)	8.53 ± 0.13 (4)	8.94 ± 0.20 (2)	8.51 ± 0.32 (6)
8	O			8.97 ± 0.24 (1)		
11	Na			5.74 ± 0.24 (1)		
12	Mg	7.95 ± 0.39 (6)	7.82 ± 0.22 (6)	8.05 ± 0.15 (5)	7.97 ± 0.36 (3)	7.85 ± 0.50 (6)
14	Si	6.60 ± 0.18 (2)	7.18 ± 0.33 (3)	7.50 ± 0.10 (3)	6.49 ± 0.20 (2)	7.23 ± 0.28 (3)
16	S					
20	Ca	6.45 ± 0.10 (3)	6.20 ± 0.28 (12)	6.96 ± 0.28 (7)	6.30 ± 0.26 (3)	6.38 ± 0.35 (7)
21	Sc	2.81 ± 0.18 (2)	3.37 ± 0.53 (3)	3.63 ± 0.32 (3)	3.65 ± 0.35 (3)	3.93 ± 0.37 (3)
22	Ti	5.02 ± 0.16 (8)	4.87 ± 0.30 (23)	5.22 ± 0.31 (11)	5.17 ± 0.23 (9)	5.40 ± 0.45 (15)
23	V		3.80 ± 0.48 (4)	4.36 ± 0.20 (2)	5.35 ± 0.23 (1)	4.91 ± 0.32 (2)
24	Cr	5.57 ± 0.14 (6)	5.29 ± 0.20 (12)	5.86 ± 0.14 (8)	5.96 ± 0.18 (6)	5.84 ± 0.23 (9)
25	Mn		4.91 ± 0.22 (2)	5.86 ± 0.20 (2)	5.45 ± 0.22 (2)	5.58 ± 0.32 (2)
26	Fe	7.47 ± 0.12 (23)	7.23 ± 0.16 (45)	7.63 ± 0.18 (33)	7.51 ± 0.24 (14)	7.58 ± 0.18 (31)
28	Ni	6.27 ± 0.18 (1)	6.17 ± 0.27 (3)	6.942 ± 0.20 (2)	5.93 ± 0.20 (2)	6.69 ± 0.32 (2)
29	Cu					
30	Zn		4.42 ± 0.20 (1)			
38	Sr	1.97 ± 0.18 (1)	1.54 ± 0.22 (1)	2.11 ± 0.20 (1)		
39	Y		4.64 ± 0.22 (1)	4.80 ± 0.20 (1)	4.03 ± 0.32 (1)	4.66 ± 0.32 (1)
40	Zr		2.22 ± 0.22 (1)			
56	Ba	2.74 ± 0.18 (1)	1.97 ± 0.22 (2)	2.89 ± 0.20 (2)	3.27 ± 0.32 (1)	3.43 ± 0.32 (1)

Table A2 – continuation

Atomic number	Elements	KIC 3868032	KIC 4677684	KIC 4768677	KIC 5180796	KIC 5630362
6	C	8.30 ± 0.20 (1)	8.60 ± 0.27 (2)	7.99 ± 0.13 (1)	8.66 ± 0.10 (5)	8.74 ± 0.31 (1)
8	O		8.64 ± 0.27 (1)	8.31 ± 0.24 (1)	8.83 ± 0.25 (1)	
11	Na					
12	Mg	7.93 ± 0.16 (4)	7.85 ± 0.33 (8)		8.10 ± 0.13 (5)	7.87 ± 0.51 (5)
14	Si	6.42 ± 0.20 (2)	7.54 ± 0.35 (7)		7.44 ± 0.21 (5)	6.45 ± 0.31 (2)
16	S					
20	Ca	6.57 ± 0.20 (1)	6.25 ± 0.11 (10)	6.96 ± 0.28 (7)	6.55 ± 0.28 (9)	5.85 ± 0.46 (3)
21	Sc	3.01 ± 0.20 (1)	3.52 ± 0.17 (4)	3.63 ± 0.32 (3)	3.49 ± 0.32 (5)	2.15 ± 0.31 (1)
22	Ti	4.77 ± 0.17 (6)	5.17 ± 0.19 (30)	5.22 ± 0.31 (11)	5.36 ± 0.32 (14)	4.99 ± 0.13 (6)
23	V			4.36 ± 0.20 (2)	4.81 ± 0.25 (2)	
24	Cr	5.53 ± 0.26 (5)	5.72 ± 0.24 (15)	5.11 ± 0.14 (5)	5.93 ± 0.12 (10)	5.59 ± 0.21 (6)
25	Mn		5.73 ± 0.44 (3)		5.50 ± 0.26 (3)	4.38 ± 0.31 (1)
26	Fe	7.11 ± 0.16 (12)	7.52 ± 0.16 (55)	6.94 ± 0.18 (17)	7.73 ± 0.17 (39)	7.34 ± 0.23 (20)
28	Ni	6.27 ± 0.18 (1)	6.08 ± 0.48 (3)		6.51 ± 0.26 (4)	
29	Cu					
30	Zn					
38	Sr		2.61 ± 0.27 (1)		1.99 ± 0.25 (1)	
39	Y		2.22 ± 0.27 (2)		3.83 ± 0.25 (1)	
40	Zr				3.22 ± 0.25 (1)	
56	Ba	1.98 ± 0.20 (1)	2.48 ± 0.20 (2)		2.44 ± 0.25 (2)	2.71 ± 0.31 (1)

Table A2 – continuation

Atomic number	Elements	KIC 6199731	KIC 6500578	KIC 6776331	KIC 7694191	KIC 7732458
6	C	8.72 ± 0.23 (1)	8.41 ± 0.15 (8)	8.71 ± 0.27 (7)	8.76 ± 0.27 (5)	8.79 ± 0.15 (7)
8	O		8.68 ± 0.32 (2)			8.20 ± 0.28 (2)
11	Na		6.54 ± 0.32 (1)			6.48 ± 0.28 (1)
12	Mg	7.00 ± 0.23 (3)	7.84 ± 0.29 (8)	8.03 ± 0.12 (7)	7.68 ± 0.18 (3)	8.24 ± 0.26 (5)
14	Si	6.67 ± 0.23 (2)	6.97 ± 0.48 (9)	7.07 ± 0.32 (10)	6.90 ± 0.49 (4)	7.59 ± 0.28 (10)
16	S					
20	Ca	5.88 ± 0.39 (3)	6.40 ± 0.30 (11)	6.86 ± 0.28 (21)	6.27 ± 0.18 (8)	6.73 ± 0.35 (21)
21	Sc	2.69 ± 0.23 (1)	3.12 ± 0.35 (4)	3.22 ± 0.22 (6)	3.12 ± 0.21 (7)	3.45 ± 0.31 (7)
22	Ti	4.97 ± 0.25 (9)	5.00 ± 0.23 (22)	5.43 ± 0.22 (37)	5.23 ± 0.25 (27)	5.45 ± 0.31 (30)
23	V		3.90 ± 0.35 (3)	4.58 ± 0.29 (4)		4.66 ± 0.21 (3)
24	Cr	5.62 ± 0.26 (7)	5.65 ± 0.26 (18)	5.80 ± 0.30 (29)	5.65 ± 0.27 (13)	6.01 ± 0.30 (30)
25	Mn	4.73 ± 0.23 (2)	5.11 ± 0.61 (6)	5.46 ± 0.23 (9)	5.58 ± 0.42 (6)	5.83 ± 0.21 (10)
26	Fe	7.23 ± 0.10 (15)	7.35 ± 0.17 (47)	7.65 ± 0.16 (102)	7.31 ± 0.25 (59)	7.73 ± 0.21 (89)
28	Ni		6.37 ± 0.43 (12)	6.25 ± 0.32 (21)	6.18 ± 0.25 (7)	6.51 ± 0.38 (32)
29	Cu					4.61 ± 0.28 (2)
30	Zn					
38	Sr		3.16 ± 0.32 (1)	3.96 ± 0.31 (2)	2.43 ± 0.24 (1)	3.55 ± 0.28 (2)
39	Y		2.34 ± 0.32 (2)	3.45 ± 0.57 (3)	2.73 ± 0.24 (2)	2.53 ± 0.20 (4)
40	Zr		2.86 ± 0.33 (5)	3.40 ± 0.76 (5)	3.04 ± 0.24 (1)	3.04 ± 0.39 (3)
56	Ba	2.38 ± 0.23 (1)	2.55 ± 0.21 (3)	3.22 ± 0.31 (1)	1.98 ± 0.24 (1)	3.09 ± 0.18 (2)

Table A2 – continuation

Atomic number	Elements	KIC 9052363	KIC 9775385	KIC 10281360	KIC 11197934	KIC 11199412
6	C	8.80 ± 0.14 (3)	8.75 ± 0.10 (6)	8.75 ± 0.25 (4)	8.95 ± 0.37 (1)	8.82 ± 0.21 (2)
8	O		8.96 ± 0.24 (1)	8.67 ± 0.25 (1)		8.34 ± 0.21 (1)
11	Na		5.96 ± 0.24 (1)	6.16 ± 0.25 (1)		
12	Mg	7.56 ± 0.10 (4)	7.96 ± 0.17 (5)	7.48 ± 0.22 (5)	8.09 ± 0.37 (2)	6.68 ± 0.14 (3)
14	Si	7.23 ± 0.23 (6)	7.16 ± 0.38 (21)	7.01 ± 0.10 (3)	7.04 ± 0.37 (2)	6.07 ± 0.21 (2)
16	S		6.99 ± 0.24 (2)			
20	Ca	6.20 ± 0.22 (8)	6.37 ± 0.29 (17)	6.35 ± 0.19 (9)	6.27 ± 0.52 (5)	5.86 ± 0.24 (5)
21	Sc	2.98 ± 0.15 (6)	2.94 ± 0.22 (12)	2.96 ± 0.12 (6)	4.35 ± 0.70 (3)	2.18 ± 0.21 (2)
22	Ti	5.04 ± 0.34 (23)	5.06 ± 0.22 (40)	4.86 ± 0.31 (29)	5.05 ± 0.23 (8)	4.64 ± 0.35 (19)
23	V	4.36 ± 0.22 (2)	4.71 ± 0.19 (6)	4.03 ± 0.28 (4)	4.35 ± 0.37 (1)	3.67 ± 0.12 (3)
24	Cr	5.64 ± 0.26 (13)	5.75 ± 0.19 (26)	5.46 ± 0.29 (15)	5.75 ± 0.18 (8)	5.03 ± 0.21 (7)
25	Mn	5.45 ± 0.13 (3)	5.66 ± 0.30 (11)	5.16 ± 0.25 (2)	5.38 ± 0.37 (2)	5.03 ± 0.13 (4)
26	Fe	7.40 ± 0.19 (42)	7.44 ± 0.17 (90)	7.29 ± 0.14 (48)	7.46 ± 0.21 (15)	6.68 ± 0.24 (36)
28	Ni	6.35 ± 0.17 (6)	6.33 ± 0.36 (27)	6.12 ± 0.14 (13)	6.35 ± 0.37 (1)	5.73 ± 0.24 (3)
29	Cu		3.50 ± 0.24 (2)			
30	Zn					
38	Sr	2.11 ± 0.22 (1)	3.13 ± 0.24 (2)			
39	Y	2.65 ± 0.22 (2)	2.51 ± 0.31 (5)	2.56 ± 0.63 (4)		2.36 ± 0.21 (2)
40	Zr	3.14 ± 0.22 (2)	3.30 ± 0.10 (5)	2.45 ± 0.25 (2)		
56	Ba	2.09 ± 0.22 (2)	1.99 ± 0.17 (3)	2.27 ± 0.25 (2)	3.66 ± 0.37 (2)	1.47 ± 0.21 (2)

Table A2 – continuation

Atomic number	Elements	KIC 11508397	KIC 11612274	KIC 11718839	KIC 11822666
6	C	8.89 ± 0.31 (1)	8.30 ± 0.22 (6)	8.64 ± 0.15 (6)	8.95 ± 0.37 (1)
8	O			8.82 ± 0.25 (1)	
11	Na				
12	Mg	8.17 ± 0.21 (4)	7.86 ± 0.10 (4)	7.93 ± 0.18 (5)	8.09 ± 0.37 (2)
14	Si	6.72 ± 0.31 (2)	7.41 ± 0.10 (3)	7.25 ± 0.40 (10)	7.04 ± 0.37 (2)
16	S				
20	Ca	7.73 ± 0.41 (4)	6.57 ± 0.39 (9)	6.45 ± 0.15 (17)	6.27 ± 0.52 (5)
21	Sc		3.33 ± 0.29 (5)	3.31 ± 0.35 (14)	4.35 ± 0.70 (3)
22	Ti	5.21 ± 0.34 (7)	4.96 ± 0.28 (19)	5.17 ± 0.15 (40)	5.05 ± 0.23 (8)
23	V	4.13 ± 0.31 (1)	4.04 ± 0.25 (2)	4.40 ± 0.25 (2)	4.35 ± 0.37 (1)
24	Cr	5.69 ± 0.36 (5)	5.50 ± 0.28 (12)	5.75 ± 0.17 (24)	5.75 ± 0.18 (8)
25	Mn	5.07 ± 0.31 (1)	5.34 ± 0.25 (2)	5.64 ± 0.14 (5)	5.38 ± 0.37 (2)
26	Fe	7.68 ± 0.19 (23)	7.38 ± 0.14 (36)	7.45 ± 0.15 (106)	7.46 ± 0.21 (15)
28	Ni	6.31 ± 0.31 (2)	6.09 ± 0.34 (10)	6.21 ± 0.14 (15)	6.35 ± 0.37 (1)
29	Cu				
30	Zn				
38	Sr	1.65 ± 0.31 (1)	3.09 ± 0.24 (1)	2.53 ± 0.12 (3)	
39	Y		2.23 ± 0.31 (2)	2.21 ± 0.19 (3)	
40	Zr		3.36 ± 0.10 (2)	3.11 ± 0.19 (4)	
56	Ba	1.84 ± 0.31 (1)	2.73 ± 0.17 (2)	2.24 ± 0.10 (3)	3.66 ± 0.37 (2)

Table A3. The atmospheric parameters of the stars that have low-resolution spectroscopy in the literature.

KIC	T_{eff} (K)	$\log g$ (dex)	Fe/H (dex)	Reference
4677684	9245 ± 529	3.82 ± 0.13	− 0.19 ± 0.13	1
4768677	9655 ± 323	3.82 ± 0.12	− 0.22 ± 0.12	1
5180796	7981 ± 370	3.87 ± 0.13	− 0.12 ± 0.12	1
	8090 ± 10	3.80	− 0.04	2
6199731	7390 ± 255	3.96 ± 0.13	− 0.08 ± 0.13	1
7694191	8140 ± 10	3.79	− 0.14	2
9052363	7752 ± 320	3.90 ± 0.12	− 0.10 ± 0.13	1
9775385	7296 ± 137	3.89 ± 0.13	0.06 ± 0.14	1
10281360	7300 ± 10	4.04	− 0.03	2
11197934	7429 ± 205	3.90 ± 0.12	0.00 ± 0.13	1
11199412	11956 ± 1854	4.00 ± 0.15	0.05 ± 0.16	1
11508397	7300 ± 148	3.91 ± 0.14	0.02 ± 0.13	1
11612274	7179 ± 152	4.01 ± 0.13	− 0.03 ± 0.13	1
	7175 ± 16	4.07 ± 0.02	− 0.21 ± 0.01	2
11718839	7734 ± 210	3.82 ± 0.12	− 0.07 ± 0.12	1

Note. References: 1. Frasca et al. (2016), 2. Qian et al. (2019).

This paper has been typeset from a $\text{\TeX}/\text{\LaTeX}$ file prepared by the author.